

## Article

# A Hybrid Approach for Extracting Large-Scale and Accurate Built-Up Areas Using SAR and Multispectral Data

Rida Azmi <sup>1,\*</sup> , Jérôme Chenal <sup>1,2</sup> , Hicham Amar <sup>3</sup>, Cédric Stéphane Tekouabou Koumetio <sup>1</sup>   
and El Bachir Diop <sup>1</sup>

- <sup>1</sup> Center of Urban Systems—CUS, Mohammad VI Polytechnic University, Ben Guerir 43150, Morocco  
<sup>2</sup> Urban and Regional Planning Community (CEAT), Ecole Polytechnique Federale de Lausanne (EPFL), 1015 Lausanne, Switzerland  
<sup>3</sup> Geology and Sustainable Mining Institute (GSMI), Mohammed VI Polytechnic University (UM6P), Ben Guerir 43150, Morocco  
\* Correspondence: rida.azmi@um6p.ma

**Abstract:** This article examines the use of multisensor data fusion for land classification in three Moroccan cities. The method employs a Random Forest classification algorithm based on multispectral, synthetic aperture radar (SAR), and derived land surface temperature (LST) data. The study compares the proposed approach to existing datasets on impervious surfaces (Global Artificial Impervious Area—GAIA, Global Human Settlement Layer—GHSL, and Global 30 m Impervious Surfaces Dynamic Dataset—GIS30D) using traditional evaluation metrics and a common training and validation dataset. The results indicate that the proposed approach has a higher precision (as measured by the F-score) than the existing datasets. The results of this study could be used to improve current databases and establish an urban data hub for impervious surfaces in Africa. The dynamic information of impervious surfaces is useful in urban planning as an indication of the intensity of human activities and economic development.

**Keywords:** built-up areas; data fusion; LST; SAR data; multispectral; impervious surfaces



**Citation:** Azmi, R.; Chenal, J.; Amar, H.; Tekouabou Koumetio, C.S.; Diop, E.B. A Hybrid Approach for Extracting Large-Scale and Accurate Built-Up Areas Using SAR and Multispectral Data. *Atmosphere* **2023**, *14*, 240. <https://doi.org/10.3390/atmos14020240>

Academic Editors: Geng-Ming Jiang and Bo-Hui Tang

Received: 4 December 2022

Revised: 15 January 2023

Accepted: 19 January 2023

Published: 25 January 2023



**Copyright:** © 2023 by the authors. Licensee MDPI, Basel, Switzerland. This article is an open access article distributed under the terms and conditions of the Creative Commons Attribution (CC BY) license (<https://creativecommons.org/licenses/by/4.0/>).

## 1. Introduction

Applications of remote sensing range from monitoring urban dynamics, such as traffic patterns, urban sprawl, or land use changes, to assisting decision-making and planning processes for humanitarian crises and emergency responses [1]. It is a complex and small-scale environment that is often characterized by a high degree of heterogeneity. Satellite imagery can express urban structure at various levels of detail depending on the demanded scale.

Because cities house most of the world's population, large-scale spatial remote sensing applications for urban settlement are critical. As a result, it is essential to discuss multimodal RF strategies and methods in the context of urban remote sensing [2]. However, unifying information from multimodal sensors in urban applications has long been desired but has proven difficult to achieve [3,4].

There are many studies that use high and medium resolution remote sensing data to understand the changes and evolution of urban areas over time and to support the implementation of sustainable development goals, particularly goal number 11.3 [5]. These studies have helped to improve our understanding of urban dynamics and have developed methods and approaches to achieve these goals. In addition, various initiatives have been undertaken to share Earth observation-based data, models, systems, tools, and services with the public to support the UN's Sustainable Development Goals [5–7].

Because urbanization involves the growth and development of urban areas, it frequently results in changes in land use, land cover, and the built environment. However, accurate information on the size and spatial distribution of urban areas is required to

make more effective decisions about the extent and consequences of urban transformation. Existing global datasets, such as optical and radar imagery, are widely used to measure, analyze, and comprehend the complex processes of urbanization, as well as perform spatiotemporal monitoring. Nighttime light data, when compared to daytime data, are a valuable data source for determining urban sprawl, despite some limitations in spatial and spectral resolution [8].

Synthetic aperture radar (SAR) data are also used to determine urban expansion and urban objects, with several studies having shown that it is effective in detecting impervious surfaces with high accuracy [9–12]. Multispectral imagery has also proved to be a good product, where the observation of urban areas over time with satellite imagery can also be used to predict future growth. Satellite remote sensing sensors typically have multiple spectral bands for use in analysis; each band can be advantageous due to the properties of materials that can be identified in different parts of the light spectrum [13,14]. All these technologies have enabled the creation of databases for spatiotemporal monitoring of city development.

The use of medium resolution land resources satellites, specifically Landsat 4, 5, 7, 8, and 9, has been common in the mapping of land use land cover (LULC) data due to their free availability and effective spectral capabilities. These satellites have been utilized since 1972 to monitor changes in land use at local and regional scales, with consistent temporal coverage and a spatial resolution of 30 m. Various techniques, including spectral indices [15–17], multispectral classification [18,19], and hybrid approaches incorporating multispectral and thermal bands, have been employed to extract constructed surfaces from these images [20,21].

The ability to monitor changes in land use and land cover over time has greatly increased with the availability of high-resolution satellite data from Landsat and Sentinel-2 [22–24]. These satellites provide multiple spectral bands that can be used to identify materials and track changes in the built environment. The use of cloud-based processing platforms such as Google Earth Engine has also made it easier and more cost-effective for researchers to access and analyze large-scale data [25]. While these advancements have greatly expanded the potential for Earth observation and geospatial research, there are still opportunities to further improve the use of such technologies, particularly in developing countries [26].

### *1.1. Motivation of the Study*

In an African context, much of what happens in African cities is invisible or only partially visible, and most of it goes unrecorded [27]. African cities with 30–80% of their population living in informal settlements have little or no data. In other words, there is a knowledge gap related to the factors that create or influence cities. This is usually accompanied by a lack of maps, official street names, and registered addresses. In addition, there is also an absence of information referring to housing conditions, water supply, sanitation, drainage, basic services, etc.

In this paper, the focus will be on land use land cover (LULC) spatial data, specifically multisensor and temporal data, to propose a first workflow prototype that allows the generation of the first hybrid LULC data that provide visibility into the evolution of the urban fabric. The adopted methodology will concentrate on the ability to obtain these data with pinpoint accuracy using spatial remote sensing and the GEE cloud computing platform.

### *1.2. Correlation between Input Data*

The joint use of synthetic aperture radar (SAR) and multispectral sensors can provide detailed and accurate information about the physical, biological, and human-made features of urban areas. SAR is particularly useful for capturing information about the surface roughness and texture of urban areas, while multispectral sensors can provide information about the spectral reflectance of different materials in the urban landscape [28–31]. The urban landscape is a component of the environment that includes a complex mix of roads, buildings, parking lots, gardens, cemeteries, soil, water, and other elements. Furthermore,

to identify dynamic urban morphology, some globally accepted and widely used mathematical indices have been developed. Spectral indices, on the other hand, have made promising advances in urban LULC studies via mapping, estimation, change detection, time-series analysis, urban dynamics, monitoring, modeling, etc. [32]. Several studies have proposed indices that allow the collection of precise data on the complexity of urban space, including the Normalized Water Difference Index—NDWI, Normalized Difference Built-up Index—NDBI, and Normalized Difference Vegetation Index—NDVI [33–35].

Land surface temperature (LST) is another important data source that researchers use to study the impact of urban development on future microclimates by predicting LST distribution and simulating land use dynamics [36,37]. As a result, LST is used as an indicator to examine the spatial distribution of urban heat. However, some authors have used average-scale local building types and climate zones to demonstrate that LST has an impact on impervious surfaces [38,39]. Subsequent research has demonstrated this positive relationship between LST and impervious surfaces, as well as the upward trend used to investigate possible drivers underlying the spatiotemporal pattern of the LST–impervious surface relationship [40–42].

### *1.3. Random Forest Classifier in Remote Sensing*

Research has shown that the Random Forest (RF) classifier can effectively classify multisource remote sensing and geographic data due to its speed and ability to optimize the classification model by including only relevant input datasets. This was demonstrated in the study by Belgiu and Drăguț [43]. To improve the accuracy of the results and reduce the computational burden, it is important to carefully select the most relevant input datasets to include in the classification process. The accuracy of the Random Forest classifier can be affected by the characteristics of the training samples and the number of data dimensions. To ensure reliable results, the training and validation data should be independent, and the classes should be equally represented in the training sample. It is also important to have enough training samples, particularly when working with a large number of data dimensions, to avoid the Hughes phenomenon. The RF classifier requires two parameters to be set in order to grow the trees: the number of decision trees to be generated (Ntree) and the number of variables to be selected and tested for the best split when growing the trees (Mtry). Research has shown that the accuracy of the classification is less sensitive to the Ntree parameter than to the Mtry parameter. The RF classifier has been used successfully in mapping land cover classes using remote sensing data, where the classifier also allows for the determination of relative feature importance, which aids in the selection of the classifier's most contributing features.

### *1.4. Large Scale Data on Impervious Surfaces*

Over the last few decades, various techniques to produce regional or global multi-temporal impervious-surface products have been proposed. These approaches are broadly classified into two categories: (1) time-series change detection and (2) multitemporal independent classification and extraction. Table 1 lists available databases that have extracted impervious surfaces using moderate resolution satellite remote sensing images with large scale. Each database is unique and authors have used a variety of techniques to improve their accuracy. These listed databases were analyzed to comprehend their characteristics, spatial resolution, and availability on GEE to automate the process of calculating our hybrid approach and comparisons with the existing dataset in the following sections.

The Global Human Settlement Layer (GHSL) is a database created by the Joint Research Center of the European Commission that provides information about the built environment on the surface of the Earth. It is based on data from Landsat satellites collected between 1975 and 2014 at various spatial resolutions. The data were processed using automatic and reproducible statistical learning methods with a spatial resolution of 30 m. The final product had a resolution of 30 m and was used to monitor impervious surfaces, but it overestimated the extent of impervious surfaces and missed smaller, fragmented impervious objects. The

grid cells are classified based on the presence and intensity of built-up areas, allowing for the mapping, and understanding of urbanization patterns on a global scale. The data are useful for policymakers, researchers, and other stakeholders interested in the effects of urbanization on the environment and human well-being.

**Table 1.** List of dataset characteristics for urban footprint.

Data	Data Citation	Data Source	Availability in GEE	Resolution in Meters	Range
Global Human Settlement Layer, built-up grid	Pesaresi et al. [44]	GHSL [45]	Available in GEE	30	1975–2014
GlobeLand30	Jun et al. [46]	GLOBELAND30 [47]	Not available in GEE	30	2000–2020
GAIA	Gong et al. [48]	GAIA [49]	Available in GEE	30	1985–2018
GISD30: global 30 m impervious surface dynamic dataset from 1985 to 2020 [50]	Zhang et al. [51]	Zendo [52]	Not available in GEE	30	1985–2020

GlobeLand30 is a global land cover dataset developed by the Chinese Academy of Sciences. It provides information on land cover types, including urban areas, forests, grasslands, and agricultural lands. The data are available at a spatial resolution of 30 m and are based on Landsat satellite imagery from the year 2000. It is a widely used dataset for mapping and analyzing land cover and land use patterns on a global scale. The Ministry of Natural Resources released GlobeLand30 Update in 2017 and the most recent version is GlobeLand30 2020, which includes 10 land cover classes.

The third dataset used in this study is Global Artificial Impervious Area (GAIA). It is a collection of Landsat satellite images from the GEE archive used to track the annual changes in artificial impervious areas, or areas covered by human-made structures, from 1985 to 2018 at a spatial resolution of 30 m. This dataset is believed to have the longest available temporal coverage for artificial impervious areas worldwide. In addition, the authors claim that their approach, which includes ancillary datasets such as NTL and Sentinel SAR data, is 15% more accurate in mapping artificial impervious areas in arid regions compared to previous methods. However, the author also notes that the use of 30 m Landsat pixels, while providing a relatively high spatial resolution, can still result in uncertainties due to mixed pixels caused by the complex mixture of spectral signatures in urban environments.

The GISD30 dataset proposed an automatic method for creating a global, 30 m impervious surface dynamic dataset from 1985 to 2020. It was shown that the dataset effectively captured the spatial distribution and spatiotemporal dynamics of impervious surfaces, but it had some limitations. One issue was the assumption that the transition from pervious to impervious surfaces was irreversible, which meant that the method could not capture transitions from impervious to pervious surfaces, such as those caused by urban greening. Additionally, many changes occurred in impervious surfaces, such as demolition and reconstruction, that were not captured by the method or product.

The following lessons can be drawn from previously mentioned databases that generate impervious surfaces: (1) Combining multiple sources can improve land cover classification and extraction accuracy. (2) Noise removal can help to improve data input. (3) Spectral separability using Principal Component Analysis is one of many techniques used (PCA). The use of spectral indices for this purpose, on the other hand, allows for noise reduction at the feature space level.

The purpose of this study is to combine multiple data sources to produce highly accurate and temporally impervious surfaces. The primary goals of this study were to: (1) demonstrate that hybrid data can improve urban footprint extraction; (2) demonstrate the strong correlation between derived data such as LST and multispectral that can enhance classification accuracy; and (3) investigate, compare, and validate the accuracy of

a hybrid classified dataset by making a comparison through cross-validation with other spatiotemporal datasets.

## 2. Materials and Methods

### 2.1. Workflow for Data Processing

The proposed method entails making a classification and then comparing the results to previous databases to determine the consistency of the hybrid approach used in this study. The detailed processing chain used to extract and compare the accuracy of the new hybrid LULC data is depicted in Figure 1. The processing chain is comprised of three major steps: (1) input preprocessing and training dataset; (2) apply classification of preprocessed time-series data; and (3) compare the obtained results to those of similar existing databases.

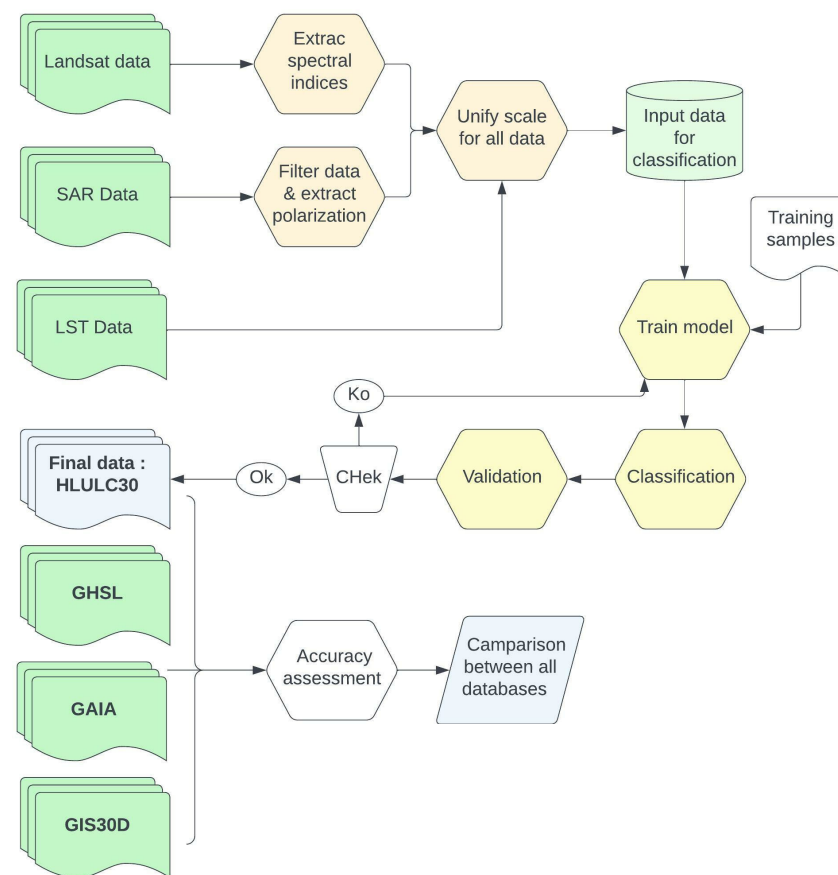


**Figure 1.** Flowchart of the study.

The processing began with the generation of medium resolution Landsat data and the calculation of the spectral indices: the vegetation index via NDVI and NDWI and the building index via NDBI. The Sentinel-1 constellation's SAR data were used as the second type of input data, with PAL SAR data used for dates earlier than 2007 [53]. The third source of data, namely, the LST derived from the archived Landsat images, was also used. The model developed by [54] was used to automate the calculation of the LST for each date. Another preprocessing step was to standardize the scale of the data used, followed by storage of these data in a new database for each date.

Following the classification and generation of thematic maps, the accuracy of the dataset was compared to previous databases, with the datasets used for comparison being GAIA, GHSL, and GIS30D, as shown in Table 1.

## 2.2. Study Area

The research area consists of the three major most densely populated Moroccan cities with distinct urban architectures. The final choice was strategic to diversify the structures and test the classification model in various areas with spatially diverse building styles. The areas represent three metropolises in the Kingdom of Morocco. The choice of these areas is due to the spatial variability that characterizes each area or region of the country. The northern zone of Morocco is characterized by a hilly terrain [55]. Today, Tangier has more than 848,337 inhabitants and occupies more than 16,000 hectares, without counting its immediate periphery, which extends to the neighboring rural municipalities. Tangier's history has been marked by the presence of several civilizational and cultural currents brought by the flows of people of various nationalities (Portuguese, Spanish, Italian, French, English, and American).

The second targeted study area, the city of Marrakech located in the heart of the Haouz Plain, is one of the oldest imperial capitals. For centuries, Marrakech was an exemplary model of a Muslim city, in the image of Baghdad and Cordoba. The urban fabric of Marrakech is defined by a series of specific architectural forms known as the *derb*. The *derb*, a fundamental component of urban morphology, represents the social link between the house and the neighborhood. Moreover, the urban structure of Marrakech appears to be a simple juxtaposition of autonomous elements grouped around a souk, which probably gives it this rural aspect, but it is no less complex in its organization, which is typical of Muslim cities and is based on the *derb*, a basic unit of measurement [56,57].

Casablanca, the third study area, already existed in the form of a city, the "Old Medina," in 1900, with more than 20,000 inhabitants spread across 47 hectares. The birth of the French city began in 1907, near the port and the old medina, with the appearance and construction of the city's nucleus, which would quickly expand. Following the establishment of the French Protectorate in 1912, the urban space of Casablanca underwent numerous changes because of major decisions made by colonial authorities, most notably establishing the city as the country's economic capital [58]. Following independence, Casablanca was left to its own devices, and its urban space was subject to fragmentation caused by spontaneous development, which peaked in the 1970s, causing it to stretch in all directions, particularly to the south and south-east, despite a few attempts at planning, which were partial in nature and lacked grand designs or a forward vision. Figure 2 depicts the geographical location of the three cities that were examined using satellite images to reveal the change in their urban fabric between 2000 and 2020, with the urban fabric depicted in magenta colors in all images, while new dates (e.g., 2020) show a dark magenta color and old dates (e.g., 2000) show a light magenta color. For OLI and TIRS data, the band combination is SWIR, NIR, and Green, while for TM data, it is SWIR, NIR, and Blue.

## 2.3. Input Data and Samples

The complexity of the urban pattern arises from the combination of vegetation, water, and built-up areas in one location. This complexity refers to the layout and organization of the built environment in an urban area, including factors such as building size and shape, development density and distribution, the presence of various land uses and infrastructure, and street network connectivity [59,60]. In order to differentiate impermeable surfaces, three spectral ratios were used to determine the pattern of urban impervious surfaces: NDVI to highlight urban vegetation, NDBI to reduce noise in the spectral bands over built-up areas, and NDWI to complement the water component in the urban ecosystem. These ratios are represented in equations (a), (b), and (c), with the wavelengths of the bands used in each sensor described in Table 2.

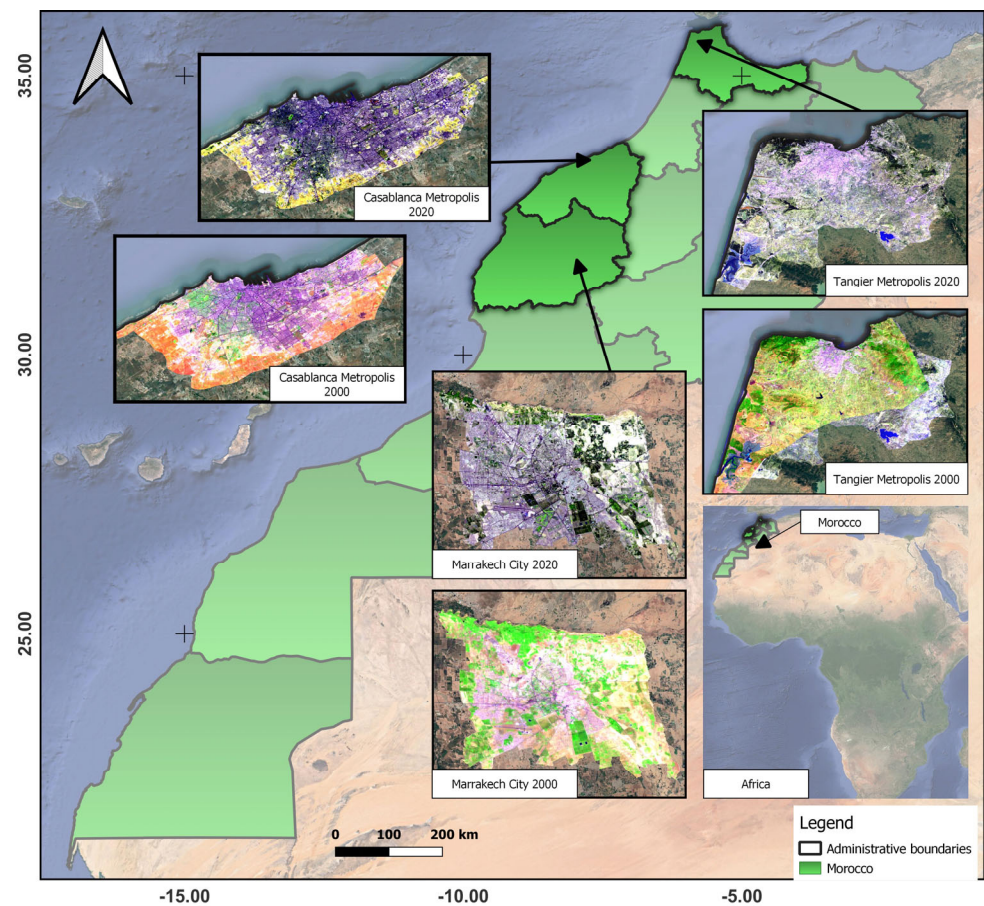


Figure 2. Study areas of located targeted cities used in the classification process.

Table 2. List of dataset characteristics for urban footprint.

Band	Landsat 8 OLI and TIRS Wavelengths in Micrometers	Landsat 5 TM Wavelength in Micrometers
NIR	Also called <b>B5</b> , with wavelengths ranging from 0.85 to 0.88	Also called <b>B4</b> , with wavelengths ranging from 0.76 to 0.90
Red	Also called <b>B4</b> , with wavelengths ranging from 0.64 to 0.67	Also called <b>B3</b> , with wavelengths ranging from 0.76 to 0.90
Green	Also called <b>B3</b> , with wavelengths ranging from 0.53 to 0.59	Also called <b>B2</b> , with wavelengths ranging from 0.63 to 0.69
SWIR	Also called <b>B6</b> , with wavelengths ranging from 1.57 to 1.65	Also called <b>B5</b> , with wavelengths ranging from 1.55 to 1.75

In this paper, the targeted classes are: (1) impervious surfaces, (2) bare soil, (3) vegetation, and (4) water. Table A1 in the Appendix A depicts the distribution of the number of samples per class, with special emphasis placed on the built-up and bare-soil classes, which frequently cause spectral confusion in medium resolution images. Residential areas are often surrounded by trees and lawns, making it difficult to extract them from Landsat images. Table 3 lists the various data sources that were used in this study to prepare input data for the supervised classification model. These data cover the range between 2000 and 2020 using Landsat archives for multispectral data, with Sentinel-1 SAR for recent years and Global SAR/PALSAR data for dates earlier than 2007. No data normalization was anticipated because the used RF model accepts a wide range of feature space [61]. On the other hand, a reducer function was used in GEE to unify the size of the pixels in all inputs.

$$NDVI = \frac{NIR - Red}{NIR + Red} \text{ (a), } NDBI = \frac{SWIR - NIR}{SWIR + NIR} \text{ (b), } NDWI = \frac{Green - SWIR}{Green + SWIR} \text{ (c) (1)}$$

The classification was performed using the Random Forest algorithm with NDVI, NDBI, NDWI, single bands (Blue, Green, Red, NIR, SWIR1), LST, Sentinel-1 data, and PALSAR data in certain dates as input features.

The training plots were created by manually classifying a randomly distributed point in each study area between 2000 and 2020, which gave a total of 4208 reference points processed manually. These samples contain the ground truth points, which are typically based on reference points generated by interpreting high resolution satellite images using Google Earth archives. For each study area, the samples covered the years 2000, 2005, 2010, 2015, and 2020. This gave us a total of 15 manually prepared samples for classification training and validation. Subsequently, the data were split into two categories (train and test), with the test set then set aside and a random selection of X% of the training data used as the actual training set, while the remaining (100-X) % were used as the validation set. In this case, X was set to 70%, and the model was trained and validated with 200 iterations using these different RF sets. This process, which is known as cross-validation, can be accomplished using a variety of methods [62].

**Table 3.** Different input data sources used in this study with ranges and resolution.

Used Data	Format	Type	Range
Landsat 5 TM collection 2 tier 1 calibrated at top-of-atmosphere (TOA) reflectance, Chander et al. [63]	Raster	Multispectral	19 April 1984 to 2011
Landsat 8 collection 1 tier 1 composite, Chander et al. [63]	Raster	Multispectral	7 April 2013 to 2022
Sentinel-1: Dual-polarization, C-band synthetic aperture radar (SAR), Filipponi [64]	Raster	Radar	October 2014 to 2022
Global SAR/PALSAR and PALSAR 2 mosaic, Shimada et al. [53]	Raster	Radar	1 January 2007 to 1 January 2021

The Gini impurity index was used in this study to show how pure a set of data is, with a lower index value indicating a higher level of purity. Table 4 shows the results of the sum of decreases in the Gini impurity index. This technique is used in decision tree algorithms to determine the best split point for a given feature. It is calculated by subtracting the Gini impurity of each child node from the parent node, and then summing the results for all possible splits of the feature. The split point with the highest sum of decreases in the Gini impurity index is chosen as the best split point for the decision tree. It is used to maximize the information gain and thus helps to make the decision tree more accurate.

According to Table 4, “Polarization VV” is the most important variable with an importance factor of 70.17, followed by “Polarization VH” with 69.89. This means that these two variables are the most powerful predictors in the dataset, providing the most information gain when used to split the decision tree.

The variable “NDVI” also has a relatively high importance factor, with a value of 68.54, indicating that it also provides a significant information gain when used to split the decision tree. On the other hand, “Elevation” and “Slope” have the lowest importance factors with values of 35.85 and 33.92, respectively, indicating that these variables provide less information gain and are thus less useful in the decision tree. However, these last two variables have been removed from the input data.

**Table 4.** Sum of decreases in Gini impurity index.

Layer	Importance Factor
Blue	58.28
Green	48.84
Red	45.65

**Table 4.** *Cont.*

Layer	Importance Factor
NIR	46.01
SWIR1	47.90
LST	39.70
Polarization VH	69.89
Polarization VV	70.17
Elevation	35.85
NDBI	62.88
NDVI	68.54
NDWI	63.78
Slope	33.92

### 3. Results and Discussion

In this study, a hybrid approach was used to depict the evolution of impervious surfaces over time by combining multiple data sources. The correctness and accuracy of the resulting map must be assessed and compared to existing databases. The sample-based validation method calculated four accuracy metrics from multitemporal impervious-surface validation samples: overall accuracy, kappa coefficient, producer accuracy (measuring commission error), and user accuracy (measuring omission error). Table 5 displays the classification result of the three study areas using four classes, with all dates and areas having an overall accuracy of more than 70%. Figure 3 shows maps of the final classification.

**Table 5.** Statistical metrics for classification of HLULC data, where 0: Built up, 1: Bare soil, 2: Vegetation, and 3: Water.

City	Date	Overall Accuracy	Kappa Coefficient	Producer Accuracy	User Accuracy
Casablanca 0: Built up 1: Bare soil 2: Vegetation 3: Water	2000	0.77	0.61	0: 0.8	0: 0.74
				1: 0.57	1: 0.75
				2: 0.84	2: 0.77
				3: 0.6	3: 1
	2005	0.8	0.68	0: 0.71	0: 0.78
				1: 0.84	1: 0.75
				2: 0.82	2: 0.82
				3: 1	3: 1
	2010	0.81	0.72	0: 0.68	0: 0.90
				1: 0.86	1: 0.89
				2: 0.92	2: 0.72
				3: 0.5	3: 0
2015	0.81	0.72	0: 0.93	0: 0.85	
			1: 0.70	1: 0.8	
			2: 0.78	2: 0.78	
			3: 1	3: 1	
2020	0.91	0.86	0: 0.87	0: 0.96	
			1: 0.92	1: 0.92	
			2: 0.95	2: 0.84	
			3: 1	3: 1	

Table 5. Cont.

City	Date	Overall Accuracy	Kappa Coefficient	Producer Accuracy	User Accuracy
Marrakech	2000	0.73	0.47	0: 0.40 1: 0.56 2: 0.90 3: 1	0: 0.81 1: 0.64 2: 0.74 3: 1
	2005	0.74	0.53	0: 0.60 1: 0.68 2: 0.83 3: 0	0: 0.70 1: 0.65 2: 0.78 3: 0
	2010	0.84	0.76	0: 0.85 1: 0.80 2: 0.86 3: 0.50	0: 0.82 1: 0.86 2: 0.84 3: 0
	2015	0.83	0.75	0: 0.90 1: 0.78 2: 0.85 3: 0.42	0: 0.81 1: 0.78 2: 0.87 3: 1
	2020	0.83	0.75	0: 0.83 1: 0.9 2: 0.91 3: 0.14	0: 0.85 1: 0.69 2: 0.89 3: 1
	Tangier	2000	0.71	0.48	0: 0.64 1: 0.5 2: 0.85
2005		0.80	0.62	0: 0.66 1: 0.63 2: 0.93 3: 0	0: 0.88 1: 0.79 2: 0.80 3: 0
2010		0.75	0.59	0: 0.66 1: 0.74 2: 0.80	0: 0.7 1: 0.83 2: 0.74
2015		0.76	0.63	0: 0.74 1: 0.66 2: 0.86 3: 0	0: 0.76 1: 0.92 2: 0.72 3: 0
2020		0.79	0.68	0: 0.71 1: 0.82 2: 0.84	0: 0.77 1: 0.88 2: 0.73

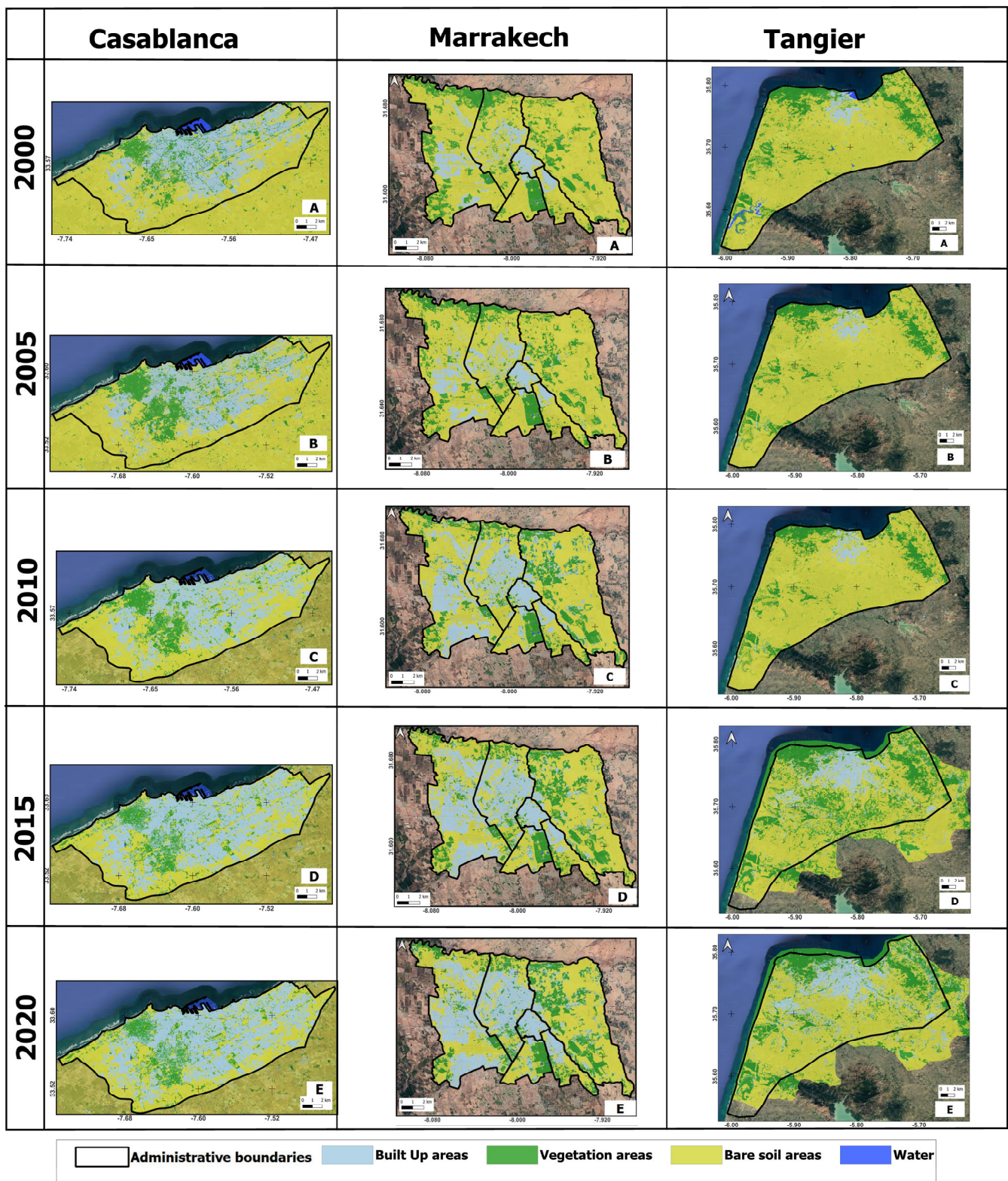


Figure 3. Thematic maps for 3 targeted cities: (A) 2000, (B) 2005, (C) 2010, (D) 2015, and (E) 2020.

In terms of user accuracy, 2000 and 2005 performed poorly compared to other time-series data (2010, 2015, and 2020). The difference can be explained by the different sensors used between the dates 2000, 2005, and 2010 and the periods 2015–2020. However, this finding will be validated in the second analysis and tested in the following sections.

### 3.1. Evaluation Metrics and Comparison

This section includes some sensitivity analyses to demonstrate the adopted design reasoning. In this section, the obtained results are first compared to those of several previously mentioned datasets (GAIA, GHSL and GIS30D). To make comparison of the various databases easier, the multitemporal databases were converted to binary class (2: built up and 1: not built up). The same samples were then used as in the first classification to perform a binary reclassification (built up vs. not built up). Of these samples, 70% were taken randomly from initial samples.

There are numerous ways to assess a classification's thematic accuracy. The error matrix allows us to compute several accuracy metrics. In this case, the F-score with precision and recall metrics for binary classification and assessment were used. Figure 4 shows the F-score test comparison of the three databases in the three study areas. Note that the GHSL dataset is not available for all dates between 2000 and 2020. According to the results in Figure 4, the F-score for HLULC exceeds 80% in all periods, while the F-scores of the other datasets do not exceed 70% within the other scenarios.

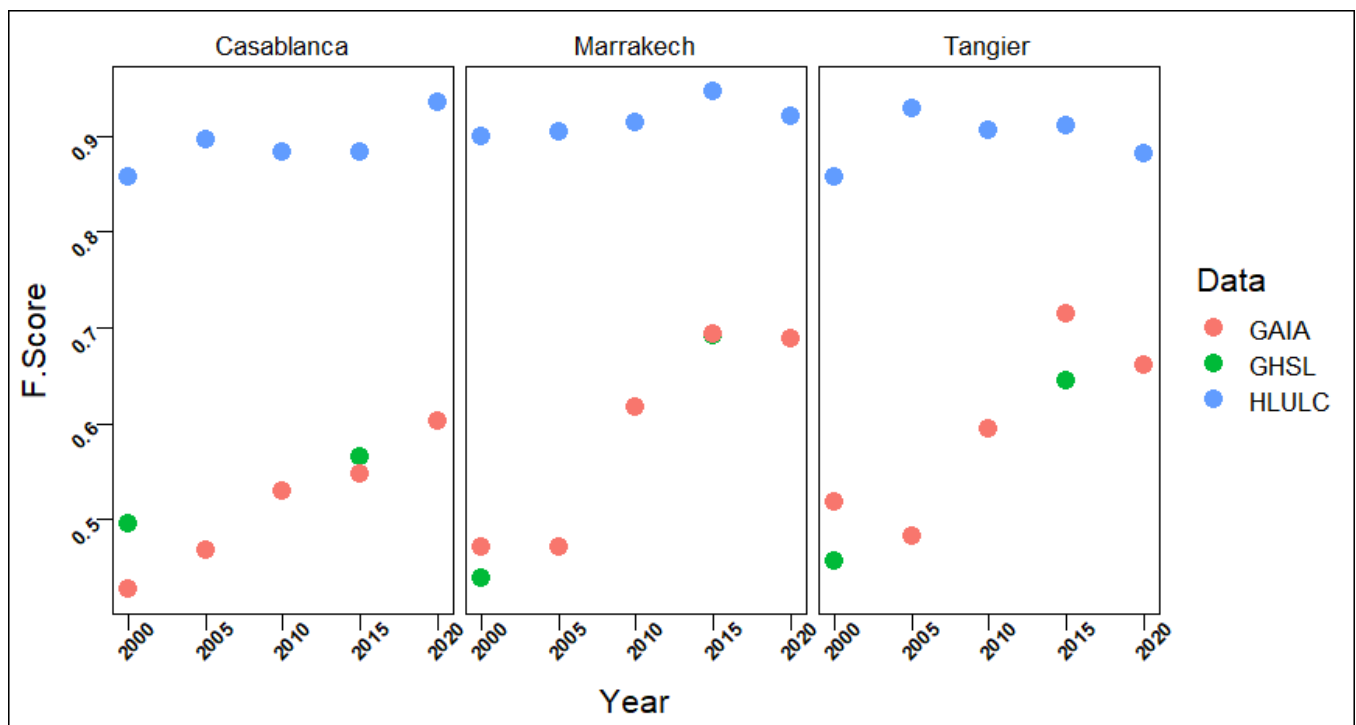


**Figure 4.** F-score in the 3 databases (GHSL, GAIA and HLULC) between 2000 and 2020.

Another comparison was made between HLULC and another database, Global 30 m Impervious Surfaces Dynamic Dataset (GIS30D). The latter is the most recent database generated on a global scale. It is a precise dynamic dataset of 30 m impervious surfaces at the global scale, based on Landsat time-series images for the period 1985 to 2020. The comparison in this study was conducted for the year 2020. As shown in Figure 5, the evaluation metrics revealed that the HLULC F-score is slightly higher than the GIS30D F-score in the three test areas. This leads to the first conclusion that in a complex feature space such as urban areas, the classification approach based on a machine learning algorithm is the most accurate compared to classical spectral indices.

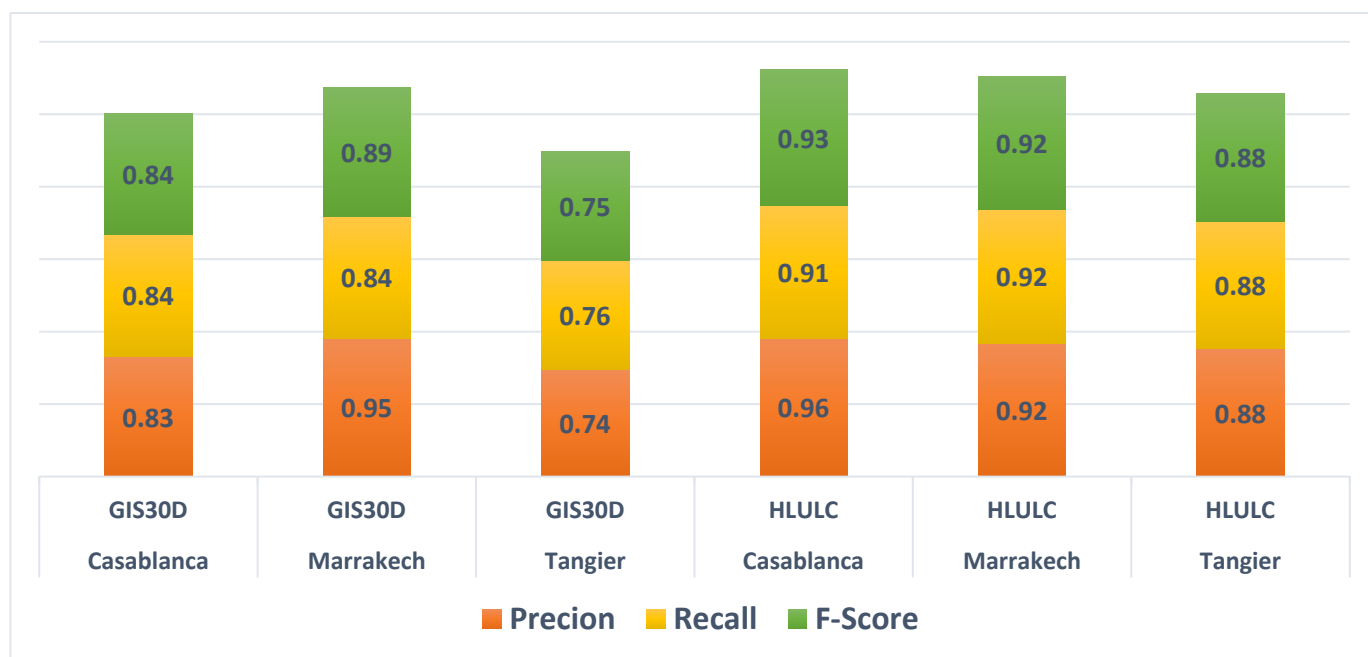


**Figure 5.** Statistical metrics using Precision, recall, and F-score between HLULC and GIS30D.

Figure 4 also shows that the F-score of all databases has a pattern in which it is slightly elevated between 2015 and 2020, and this is true for the HLULC, GAIA, and even GHSL databases. The only explanation is the quality of the spectral bands used for the last two dates (2015 and 2020). To begin with, the multispectral images, OLI and TIRS from the Landsat 8 sensor, outperformed other sensors on the same satellite, such as TM and ETM+, in terms of quality and accuracy [65]. Mancino et al. [66] demonstrated an overall good correlation between indices calculated with the two sensors (in this case, OLI and TM); however, statistically significant differences were found for almost all of the indices analyzed based on single land use classes. According to the same study, more attention should be paid to the differences between the two sensors in the evaluation of infrared (NIR and SWIR)-based indices for estimating both vegetation and soil water content, both of which are highly climate-sensitive key indicators. Thus, the Sentinel-1 sensor with the C-band demonstrated its performance in terms of distinction of built-up areas. According to [67], Sentinel-1 IW mode imagery can be used to extract built-up areas, but crowded built-up areas are easier to detect than detached houses. In this study, dual polarization has assisted in detecting buildings at different orientation angles and improved the final classification.

Although the study areas differed in terms of climate and architecture, the classification performed similarly in semi-arid-to-arid areas such as Marrakech, hilly areas with dense-to-very-dense buildings such as Tangier, peri-urban areas, scattered green spaces, and, finally, coastal areas with spatial variability in terms of building typology.

### 3.2. Visual Interpretation

The conversion of the HLULC classification result into binary data allowed us to visually compare the impervious surfaces with other databases using a very high spatial resolution satellite image as reference. Figure 6 shows a visual analysis comparing the classification results between (A) HLULC, (B) GAIA dataset, and (D) the original classification. The scenes captured demonstrate that the GAIA dataset has an overestimation of the permeable surfaces which can be confused between built and bare soil in several areas, as mentioned in the Casablanca and Marrakech scene (Figure 6). Another weak point is also mentioned in the case of Tangier, where the peri-urban areas were not extracted correctly in the GAIA database. On the other hand, the HLULC model was unable to extract the

residential areas in the neighborhoods of Casablanca where greenery is frequent, in this case, the residential areas in the neighborhoods of Anfa and Ain Diab (southeast of the city). The vegetation class dominated in these areas because the classifier was influenced by the high spectral value of NDVI combined with a low value of LST. Another source of confusion is the data’s spatial resolution, which does not allow spectrally distinguishing a built-up area in a mixed pixel [68].

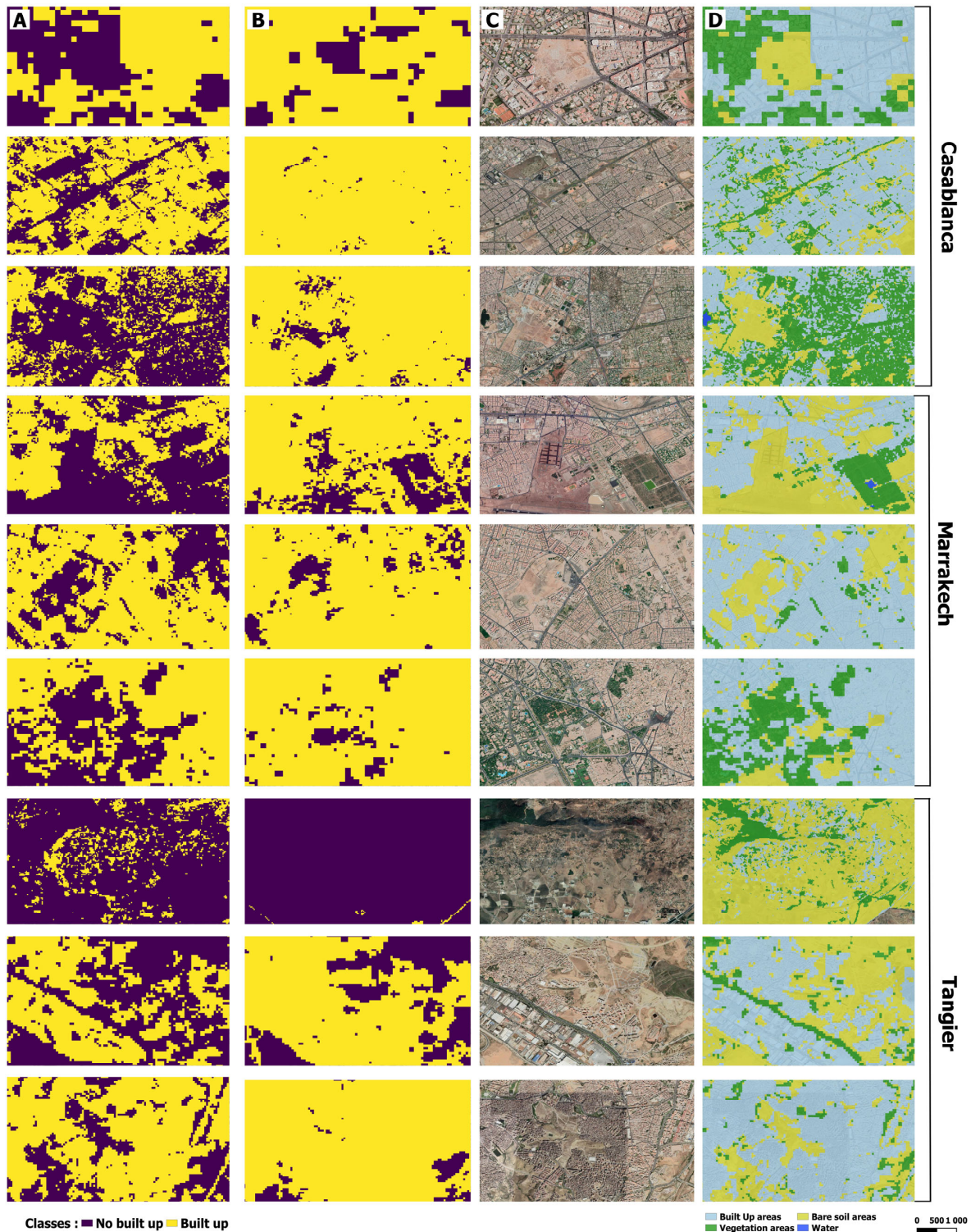


Figure 6. Visual comparison between (A) HLULC data, (B) GAIA, (C) high spatial resolution reference image, and (D) original classified image of HLULC.

Figure 6 shows that the HLULC dataset is accurate in areas with high population density and in the outskirts of cities, likely due to the inclusion of bare soil and SAR texture in the input data. The GAIA database, on the other hand, exhibits confusion in areas with low vegetation in Marrakech and Tangier. This may be due to the sensitivity of SAR backscatter to surface characteristics [69]. The findings also show the improvement of data quality caused by the multiple data sources, especially LST data and their role in enhancing classification where built-up areas are spectrally highlighted with high pixel values compared to bare soil and vegetation. However, a limitation of the proposed method is in the data preprocessing, while the image classification strategy builds classifiers for identifying impervious surfaces using training samples and performed well in complex impervious-surface mapping. However, collecting training samples, on the other hand, is a time-consuming and labor-intensive task, particularly for large-area time-series impervious-surface monitoring [70].

The major multispectral bands (RGB bands, NIR, and SWIR) were used, as well as three spectral indices (NDVI, NDWI, and NDBI), which are derivatives of the multispectral and thermal bands (LST data), and radar data from the Sentinel-1 C-band sensor with VH and VV polarization. This combination resulted in a more complex feature space, allowing the RF classifier to produce more accurate classes.

#### 4. Conclusions and Perspectives

A machine learning algorithm was used to extract a land cover map with such accuracy using a hybrid approach based on multisource data. Even with a medium resolution, the classification approach bore fruit in terms of product quality. In some cases, the SAR assisted in improving the distinction between bare soil and impervious areas. In this case, the LST was used as additional data to improve the results and reduce confusion between the two classes (soil and built). The NDVI, in conjunction with the other indices (NDWI and DDBI), allowed for the reduction of the spectral feature space. The approach proved to be effective, but it still suffers from a lack of reference data, which consumes nearly 70% of the working time.

Future projects may allow us to generalize the workflow on a continental scale and produce a reasonably accurate land use map.

This data will serve as the foundation for a knowledge base that will be used to map the urban space, monitor the evolution of the urban fabric, and achieve SDG number 11.

This data can also be used to generate precision data for indicator 11.3.1, which generates data on the calculation of the land consumption rate to population growth rate.

Future work will generate HLULC data on a continental scale, with the objective of strengthening the knowledge base of dynamic data in relation to Africa.

The GEE platform will allow the use of other types of data (including elevation, population density, etc.) to further strengthen the feature space, and to use complicated deep learning architecture such as the U-net.

**Author Contributions:** Writing—original draft preparation, R.A. and H.A.; Writing—review and editing, E.B.D. and C.S.T.K.; Supervision, J.C.; Administration, J.C.; Funding, J.C. All authors have read and agreed to the published version of the manuscript.

**Funding:** This research received no external funding.

**Institutional Review Board Statement:** The study did not require ethical approval.

**Informed Consent Statement:** Not applicable.

**Data Availability Statement:** Not applicable.

**Conflicts of Interest:** The authors declare no conflict of interest.

## Appendix A

**Table A1.** Statistics of samples used in the classification.

Location	Built Up	Vegetation	Bare Soil	Water	Total Samples
Train_Casa_2000	64	74	169	8	315
Train_Casa_2005	75	71	162	7	315
Train_Casa_2010	94	67	146	8	315
Train_Casa_2015	75	71	162	7	315
Train_Casa_2020	112	90	98	6	306
Train_Kech_2000	103	54	106	13	276
Train_Kech_2005	49	55	167	5	276
Train_Kech_2010	87	48	133	8	276
Train_Kech_2015	103	54	106	13	276
Train_Kech_2020	113	54	96	13	276
Train_Tanger_2000	34	74	142	2	252
Train_Tanger_2005	36	63	151	2	252
Train_Tanger_2010	54	54	142	2	252
Train_Tanger_2015	89	62	100	1	252
Train_Tanger_2020	97	84	70	1	252
Total	1185	975	1950	96	4206

## References

- Wellmann, T.; Lausch, A.; Andersson, E.; Knapp, S.; Cortinovis, C.; Jache, J.; Scheuer, S.; Kremer, P.; Mascarenhas, A.; Kraemer, R.; et al. Remote sensing in urban planning: Contributions towards ecologically sound policies? *Landsc. Urban Plan.* **2020**, *204*, 103921. [\[CrossRef\]](#)
- Wentz, E.A.; Anderson, S.; Fragkias, M.; Netzband, M.; Mesev, V.; Myint, S.W.; Quattrochi, D.; Rahman, A.; Seto, K.C. Supporting global environmental change research: A review of trends and knowledge gaps in urban remote sensing. *Remote Sens.* **2014**, *6*, 3879–3905. [\[CrossRef\]](#)
- Weng, Q.; Quattrochi, D.A. *Urban Remote Sensing*; CRC Press: Boca Raton, FL, USA, 2018.
- Tékouabou, S.C.K.; Chenal, J.; Azmi, R.; Toulmi, H.; Diop, E.B.; Nikiforova, A. Identifying and Classifying Urban Data Sources for Machine Learning-Based Sustainable Urban Planning and Decision Support Systems Development. *Data* **2022**, *7*, 170. [\[CrossRef\]](#)
- Wang, Y.; Huang, C.; Feng, Y.; Zhao, M.; Gu, J. Using earth observation for monitoring SDG 11.3. 1-ratio of land consumption rate to population growth rate in Mainland China. *Remote Sens.* **2020**, *12*, 357. [\[CrossRef\]](#)
- Han, L.; Lu, L.; Lu, J.; Liu, X.; Zhang, S.; Luo, K.; He, D.; Wang, P.; Guo, H.; Li, Q. Assessing Spatiotemporal Changes of SDG Indicators at the Neighborhood Level in Guilin, China: A Geospatial Big Data Approach. *Remote Sens.* **2022**, *14*, 4985. [\[CrossRef\]](#)
- Sirmacek, B.; Vinuesa, R. Remote sensing and AI for building climate adaptation applications. *Results Eng.* **2022**, *15*, 100524. [\[CrossRef\]](#)
- Baydogan, E.; Sarp, G. Urban footprint detection from night light, optical and SAR imageries: A comparison study. *Remote Sens. Appl. Soc. Environ.* **2022**, *27*, 100775. [\[CrossRef\]](#)
- Radutu, A.; Venvik, G.; Ghibus, T.; Gogu, C.R. Sentinel-1 data for underground processes recognition in Bucharest City, Romania. *Remote Sens.* **2020**, *12*, 4054. [\[CrossRef\]](#)
- Koeniguer, E.C.; Nicolas, J.-M. Change Detection Based on the Coefficient of Variation in SAR Time-Series of Urban Areas. *Remote Sens.* **2020**, *12*, 2089. [\[CrossRef\]](#)
- Marconcini, M.; Metz-Marconcini, A.; Üreyen, S.; Palacios-Lopez, D.; Hanke, W.; Bachofer, F.; Zeidler, J.; Esch, T.; Gorelick, N.; Kakarla, A.; et al. Outlining where humans live, the World Settlement Footprint 2015. *Sci. Data* **2020**, *7*, 242. [\[CrossRef\]](#) [\[PubMed\]](#)
- Mahmoud, N.; Samir, N.; Fathi, A.; Mohamed, W. *A Proposed Methodology for Detecting the Urban Footprint in Egypt*; IOP Publishing: Bristol, UK, 2022; Volume 992, p. 012008.
- Lynch, P.; Blesius, L.; Hines, E. Classification of urban area using multispectral indices for urban planning. *Remote Sens.* **2020**, *12*, 2503. [\[CrossRef\]](#)
- Benkouider, F.; Abdellaoui, A.; Hamami, L. New and improved built-up index using SPOT imagery: Application to an arid zone (Laghouat and M'Sila, Algeria). *J. Indian Soc. Remote Sens.* **2019**, *47*, 185–192. [\[CrossRef\]](#)
- Bouzekri, S.; Lasbet, A.A.; Lachehab, A. A New Spectral Index for Extraction of Built-Up Area Using Landsat-8 Data. *J. Indian Soc. Remote Sens.* **2015**, *43*, 867–873. [\[CrossRef\]](#)
- Firozjaei, M.K.; Sedighi, A.; Kiavarz, M.; Qureshi, S.; Haase, D.; Alavipanah, S.K. Automated built-up extraction index: A new technique for mapping surface built-up areas using LANDSAT 8 OLI imagery. *Remote Sens.* **2019**, *11*, 1966. [\[CrossRef\]](#)
- Zhang, P.; Sun, Q.; Liu, M.; Li, J.; Sun, D. A strategy of rapid extraction of built-up area using multi-seasonal landsat-8 thermal infrared band 10 images. *Remote Sens.* **2017**, *9*, 1126. [\[CrossRef\]](#)
- Ma, X.; Tong, X.; Liu, S.; Luo, X.; Xie, H.; Li, C. Optimized sample selection in SVM classification by combining with DMSP-OLS, Landsat NDVI and GlobeLand30 products for extracting urban built-up areas. *Remote Sens.* **2017**, *9*, 236. [\[CrossRef\]](#)
- Yu, B.; Shu, S.; Liu, H.; Song, W.; Wu, J.; Wang, L.; Chen, Z. Object-based spatial cluster analysis of urban landscape pattern using nighttime light satellite images: A case study of China. *Int. J. Geogr. Inf. Sci.* **2014**, *28*, 2328–2355. [\[CrossRef\]](#)

20. Zhang, J.; Li, P.; Wang, J. Urban built-up area extraction from Landsat TM/ETM+ images using spectral information and multivariate texture. *Remote Sens.* **2014**, *6*, 7339–7359. [[CrossRef](#)]
21. Bramhe, V.S.; Ghosh, S.K.; Garg, P.K. Extraction of built-up areas from Landsat-8 OLI data based on spectral-textural information and feature selection using support vector machine method. *Geocarto Int.* **2020**, *35*, 1067–1087. [[CrossRef](#)]
22. Li, J.; Roy, D.P. A global analysis of Sentinel-2A, Sentinel-2B and Landsat-8 data revisit intervals and implications for terrestrial monitoring. *Remote Sens.* **2017**, *9*, 902. [[CrossRef](#)]
23. Wang, Q.; Blackburn, G.A.; Onojeghuo, A.O.; Dash, J.; Zhou, L.; Zhang, Y.; Atkinson, P.M. Fusion of Landsat 8 OLI and Sentinel-2 MSI Data. *IEEE Trans. Geosci. Remote Sens.* **2017**, *55*, 3885–3899. [[CrossRef](#)]
24. Chaves, M.E.D.; Picoli, M.C.A.; Sanches, I.D. Recent applications of Landsat 8/OLI and Sentinel-2/MSI for land use and land cover mapping: A systematic review. *Remote Sens.* **2020**, *12*, 3062. [[CrossRef](#)]
25. Shetty, S. Analysis of Machine Learning Classifiers for LULC Classification on Google Earth Engine. Master's Thesis, University of Twente, Enschede, The Netherlands, March 2019.
26. Kumar, L.; Mutanga, O. Google Earth Engine applications since inception: Usage, trends, and potential. *Remote Sens.* **2018**, *10*, 1509. [[CrossRef](#)]
27. Osuteye, E.; Johnson, C.; Brown, D. The data gap: An analysis of data availability on disaster losses in sub-Saharan African cities. *Int. J. Disaster Risk Reduct.* **2017**, *26*, 24–33. [[CrossRef](#)]
28. Ban, Y.; Jacob, A. Object-based fusion of multitemporal multiangle ENVISAT ASAR and HJ-1B multispectral data for urban land-cover mapping. *IEEE Trans. Geosci. Remote Sens.* **2013**, *51*, 1998–2006. [[CrossRef](#)]
29. Zitzlsberger, G.; Podhorányi, M.; Svatoň, V.; Lazecký, M.; Martinovič, J. Neural Network-Based Urban Change Monitoring with Deep-Temporal Multispectral and SAR Remote Sensing Data. *Remote Sens.* **2021**, *13*, 3000. [[CrossRef](#)]
30. Bechtel, B.; See, L.; Mills, G.; Foley, M. Classification of local climate zones using SAR and multispectral data in an arid environment. *IEEE J. Sel. Top. Appl. Earth Obs. Remote Sens.* **2016**, *9*, 3097–3105. [[CrossRef](#)]
31. Abdikan, S.; Bilgin, G.; Sanli, F.B.; Uslu, E.; Ustuner, M. Enhancing land use classification with fusing dual-polarized TerraSAR-X and multispectral RapidEye data. *J. Appl. Remote Sens.* **2015**, *9*, 096054. [[CrossRef](#)]
32. Li, W. Mapping Urban Impervious Surfaces by Using Spectral Mixture Analysis and Spectral Indices. *Remote Sens.* **2020**, *12*, 94. [[CrossRef](#)]
33. Zheng, Y.; Tang, L.; Wang, H. An improved approach for monitoring urban built-up areas by combining NPP-VIIRS nighttime light, NDVI, NDWI, and NDBI. *J. Clean. Prod.* **2021**, *328*, 129488. [[CrossRef](#)]
34. Khine, M.M.; Maw, Y.Y.; Win, K.M.M. Change analysis of indices (NDWI, NDVI, NDBI) for Mawlamyine City area using google earth engine. *J. Myanmar Acad. Arts Sci.* **2018**, *16*. Available online: [http://webcache.googleusercontent.com/search?q=cache:A4cvSQezDNMJ:www.maas.edu.mm/Research/Admin/pdf/16.%2520Myo%2520Myo%2520Khine%2520\(297-314\).pdf&cd=1&hl=sr-Latn&ct=clnk&gl=rs](http://webcache.googleusercontent.com/search?q=cache:A4cvSQezDNMJ:www.maas.edu.mm/Research/Admin/pdf/16.%2520Myo%2520Myo%2520Khine%2520(297-314).pdf&cd=1&hl=sr-Latn&ct=clnk&gl=rs) (accessed on 3 December 2022).
35. Chen, X.-L.; Zhao, H.-M.; Li, P.-X.; Yin, Z.-Y. Remote sensing image-based analysis of the relationship between urban heat island and land use/cover changes. *Remote Sens. Environ.* **2006**, *104*, 133–146. [[CrossRef](#)]
36. Mustafa, E.K.; Liu, G.; El-Hamid, H.T.A.; Kaloop, M.R. Simulation of land use dynamics and impact on land surface temperature using satellite data. *GeoJournal* **2021**, *86*, 1089–1107. [[CrossRef](#)]
37. Zhou, W.; Qian, Y.; Li, X.; Li, W.; Han, L. Relationships between land cover and the surface urban heat island: Seasonal variability and effects of spatial and thematic resolution of land cover data on predicting land surface temperatures. *Landsc. Ecol.* **2014**, *29*, 153–167. [[CrossRef](#)]
38. Azmi, R.; Koumetio, C.S.T.; Diop, E.B.; Chenal, J. Exploring the relationship between urban form and land surface temperature (LST) in a semi-arid region case study of Ben Guerir city—Morocco. *Environ. Chall.* **2021**, *5*, 100229. [[CrossRef](#)]
39. Azmi, R.; Saadane, A.; Kacimi, I. Estimation of spatial distribution and temporal variability of land surface temperature over Casablanca and the surroundings of the city using different Landat satellite sensor type (TM, ETM+ and OLI). *Int. J. Innov. Appl. Stud.* **2015**, *11*, 49.
40. Yang, Q.; Huang, X.; Yang, J.; Liu, Y. The relationship between land surface temperature and artificial impervious surface fraction in 682 global cities: Spatiotemporal variations and drivers. *Environ. Res. Lett.* **2021**, *16*, 024032. [[CrossRef](#)]
41. Bala, R.; Prasad, R.; Yadav, V.P. A comparative analysis of day and night land surface temperature in two semi-arid cities using satellite images sampled in different seasons. *Adv. Space Res.* **2020**, *66*, 412–425. [[CrossRef](#)]
42. Deng, C.; Wu, C. Examining the impacts of urban biophysical compositions on surface urban heat island: A spectral unmixing and thermal mixing approach. *Remote Sens. Environ.* **2013**, *131*, 262–274. [[CrossRef](#)]
43. Belgiu, M.; Drăguț, L. Random forest in remote sensing: A review of applications and future directions. *ISPRS J. Photogramm. Remote Sens.* **2016**, *114*, 24–31. [[CrossRef](#)]
44. Corbane, C.; Florczyk, A.; Pesaresi, M.; Politis, P.; Syrris, V. *GHS Built-Up Grid, Derived from Landsat, Multitemporal (1975, 1990, 2000, 2014)*; European Commission, Joint Research Centre, JRC Data Catalogue: Brussels, Belgium, 2015.
45. GHSL. Global Human Settlement Layer. 2020. Available online: <https://ghsl.jrc.ec.europa.eu/download.php?ds=bu> (accessed on 3 December 2022).
46. Jun, C.; Ban, Y.; Li, S. Open access to Earth land-cover map. *Nature* **2014**, *514*, 434. [[CrossRef](#)] [[PubMed](#)]
47. GLOBELAND30. *Open Access to Earth Land-Cover Map*; GLOBELAND30: Beijing, China, 2020. [[CrossRef](#)]

48. Gong, P.; Li, X.; Wang, J.; Bai, Y.; Chen, B.; Hu, T.; Liu, X.; Xu, B.; Yang, J.; Zhang, W.; et al. Annual maps of global artificial impervious area (GAIA) between 1985 and 2018. *Remote Sens. Environ.* **2020**, *236*, 111510. [[CrossRef](#)]
49. GAIA. *Annual Maps of Global Artificial Impervious Area (GAIA)*; GAIA: Louisville, CO, USA, 2020. [[CrossRef](#)]
50. Liangyun, L.; Xiao, Z.; Xidong, C.; Yuan, G.; Jun, M. *GLC\_FCS30-2020: Global Land Cover with Fine Classification System at 30 m in 2020*; Zenodo: Geneva, Switzerland, 2020. [[CrossRef](#)]
51. Zhang, X.; Liu, L.; Zhao, T.; Gao, Y.; Chen, X.; Mi, J. GISD30: Global 30 m impervious-surface dynamic dataset from 1985 to 2020 using time-series Landsat imagery on the Google Earth Engine platform. *Earth Syst. Sci. Data* **2022**, *14*, 1831–1856. [[CrossRef](#)]
52. Zenodo. *GISD30: Global 30-m Impervious Surface Dynamic Dataset from 1985 to 2020 Using Time-Series Landsat Imagery on the Google Earth Engine Platform*; Zenodo: Geneva, Switzerland, 2020. [[CrossRef](#)]
53. Shimada, M.; Itoh, T.; Motooka, T.; Watanabe, M.; Shiraiishi, T.; Thapa, R.; Lucas, R. New global forest/non-forest maps from ALOS PALSAR data (2007–2010). *Remote Sens. Environ.* **2014**, *155*, 13–31. [[CrossRef](#)]
54. Ermida, S.L.; Soares, P.; Mantas, V.; Götsche, F.-M.; Trigo, I.F. Google earth engine open-source code for land surface temperature estimation from the landsat series. *Remote Sens.* **2020**, *12*, 1471. [[CrossRef](#)]
55. Azmi, R.; Amar, H.; Kacimi, I. Photovoltaic Site Suitability Analysis using Analytical Hierarchy Process and Sensitivity Analysis Methods with GIS and Remote Sensing in Southern Morocco: Case of Draa-Tafilaliet Region. In Proceedings of the 2017 International Renewable and Sustainable Energy Conference (IRSEC), Tangier, Morocco, 4–7 December 2017; pp. 1–5.
56. Sebti, M. *Gens de Marrakech: Géo-Démographie de la Ville Rouge*; INED: Paris, France, 2009.
57. Azmi, R.; Amar, H.; Chenal, J.; Diop, E.B.; Koumetio, C.S.T. Decision analysis related to solar farm investments based on analysis hierarchical process and fuzzy AHP for sustainable energy production. *Int. J. Energy Res.* **2022**, *46*, 11730–11755. [[CrossRef](#)]
58. Hassani, N. *La Sur-Urbanisation de la Ville de Casablanca: Étude de L'évolution Spatio-Temporelle de la Ville de Casablanca entre 1987 et 2017*. Master's Thesis, University of Lorraine, Metz, France, 2017.
59. Baranwal, E.; Ahmad, S. *Retrieving Spatial Pattern of Urban Using Spectral Ratios for Major Features of an Urban Ecosystem with Satellite Image Processing*; IOP Publishing: Bristol, UK, 2021; Volume 795, p. 012034.
60. Azmi, R.; Alami, O.B.; Saadane, A.E.; Kacimi, I.; Chafiq, T. A modified and enhanced normalized built-up index using multispectral and thermal bands. *Indian J. Sci. Technol.* **2016**, *9*, 1–11. [[CrossRef](#)]
61. Parmar, A.; Katariya, R.; Patel, V. *A Review on Random Forest: An Ensemble Classifier*; Springer: Berlin/Heidelberg, Germany, 2018; pp. 758–763.
62. Battineni, G.; Sagaro, G.G.; Nalini, C.; Amenta, F.; Tayebati, S.K. Comparative machine-learning approach: A follow-up study on type 2 diabetes predictions by cross-validation methods. *Machines* **2019**, *7*, 74. [[CrossRef](#)]
63. Chander, G.; Markham, B.L.; Helder, D.L. Summary of current radiometric calibration coefficients for Landsat MSS, TM, ETM+, and EO-1 ALI sensors. *Remote Sens. Environ.* **2009**, *113*, 893–903. [[CrossRef](#)]
64. Filipponi, F. Sentinel-1 GRD preprocessing workflow. *Multidiscip. Digit. Publ. Inst. Proc.* **2019**, *18*, 11.
65. Poursanidis, D.; Chrysoulakis, N.; Mitrika, Z. Landsat 8 vs. Landsat 5: A comparison based on urban and peri-urban land cover mapping. *Int. J. Appl. Earth Obs. Geoinf.* **2015**, *35*, 259–269. [[CrossRef](#)]
66. Mancino, G.; Ferrara, A.; Padula, A.; Nolè, A. Cross-comparison between Landsat 8 (OLI) and Landsat 7 (ETM+) derived vegetation indices in a Mediterranean environment. *Remote Sens.* **2020**, *12*, 291. [[CrossRef](#)]
67. Chini, M.; Pelich, R.; Hostache, R.; Matgen, P. Built-up areas mapping at global scale based on adaptive parametric thresholding of Sentinel-1 intensity & coherence time series. In Proceedings of the 2017 9th International Workshop on the Analysis of Multitemporal Remote Sensing Images (MultiTemp), Brugge, Belgium, 27–29 June 2017; pp. 1–4.
68. Hsieh, P.-F.; Lee, L.C.; Chen, N.-Y. Effect of spatial resolution on classification errors of pure and mixed pixels in remote sensing. *IEEE Trans. Geosci. Remote Sens.* **2001**, *39*, 2657–2663. [[CrossRef](#)]
69. Schönbrodt-Stitt, S.; Ahmadian, N.; Kurtenbach, M.; Conrad, C.; Romano, N.; Bogena, H.R.; Vereecken, H.; Nasta, P. Statistical exploration of Sentinel-1 data, terrain parameters, and in-situ data for estimating the near-surface soil moisture in a mediterranean agroecosystem. *Front. Water* **2021**, *3*, 655837. [[CrossRef](#)]
70. Chen, X.; Cao, X.; Liao, A.; Chen, L.; Peng, S.; Lu, M.; Chen, J.; Zhang, W.; Zhang, H.; Han, G.; et al. Global mapping of artificial surfaces at 30-m resolution. *Sci. China Earth Sci.* **2016**, *59*, 2295–2306. [[CrossRef](#)]

**Disclaimer/Publisher's Note:** The statements, opinions and data contained in all publications are solely those of the individual author(s) and contributor(s) and not of MDPI and/or the editor(s). MDPI and/or the editor(s) disclaim responsibility for any injury to people or property resulting from any ideas, methods, instructions or products referred to in the content.